



Transport mechanisms of hydrothermal convection in faulted tight sandstones

Guoqiang Yan; Benjamin Busch; Robert Egert; Morteza Esmaeilpour; Kai Stricker; Thomas Kohl

Institute of Applied Geosciences, Karlsruhe Institute of Technology (KIT), Karlsruhe, 76131, Germany

5 *Correspondence to:* Guoqiang Yan (guoqiang.yan@kit.edu)

Abstract. Motivated by the unknown reasons for a kilometer-scale high-temperature overprint of 270 ~ 300 °C in a reservoir outcrop analog (Piesberg Quarry, northwest Germany), numerical simulations are conducted to identify the transport mechanisms of the fault-related hydrothermal convection system. The system mainly consists of a main fault and a sandstone reservoir in which transfer faults are embedded. The results show that the buoyancy-driven convection in the main fault is the basic requirement for elevated temperatures in the reservoir. We studied the effects of permeability variations and lateral regional flow on the preferential fluid flow pathways, dominant heat transfer types, and mutual interactions among different convective and advective flow modes. The sensitivity analysis of permeability variations indicates that lateral convection in the sandstone and advection in the transfer faults can efficiently transport fluid and heat, thus causing elevated temperatures (≥ 269 °C) in the reservoir compared to purely conduction-dominated heat transfer (≤ 250 °C). Higher-level lateral regional flow interacts with convection and advection and changes the dominant heat transfer from conduction to advection in the transfer faults for the low permeability cases of sandstone and main fault. Simulations with anisotropic permeabilities detailed the dependence of the onset of convection and advection in the reservoir on the directional permeability distribution. The depth-dependent permeabilities of the main fault reduce the amount of energy transferred by buoyancy-driven convection. The increased heat and fluid flows resulting from the anisotropic main fault permeability provide the most realistic explanation for the thermal anomalies in the reservoir. Our numerical models can facilitate exploration and exploitation workflows to develop positive thermal anomalies zones as geothermal reservoirs. These preliminary results will stimulate further petroleum and geothermal studies of fully coupled thermo-hydro-mechanical-chemical processes in faulted tight sandstones.

1 Introduction

Thermal anomalies in sedimentary basins are common geological phenomena and may affect hydrocarbon reservoir properties and the utilization of subsurface space concerning porosity and permeability due to cementation with temperature-related authigenic cement (Baillieux et al., 2013). Meanwhile, the thermal anomalies in sedimentary basins can be targeted as geothermal resources for heat and electricity production (Moeck, 2014). In general, thermal anomalies may be caused by variations of thermal conductivities around structures such as salt domes (O'Brien and Lerche, 1988; Magri et al., 2008), geological/tectonic activity (Emry et al., 2020), geochemical reactions (Elderfield et al., 1999), or hydrothermal activities in faults and fractures (Cherubini et al., 2013). Indeed, in addition to being a possible cause of thermal anomalies (Zwingmann et al., 1998, 1999; Liewig and Clauer, 2000; Will et al., 2016), the hydrothermal activities in faults and fractures are often invoked to explain natural processes in sedimentary basins, such as hydrothermal mineralization (Kühn and Gessner, 2009; Harcouët-Menou et al., 2009). The common driving force for hydrothermal activities in faulted and fractured lithologies is the fluid density difference caused by temperature variations (Nield and Bejan, 2017). The resulting process is called buoyancy-driven convection/flow. Many numerical models imply that buoyancy-driven convection in faulted basins could explain the correlation between faulted zones or adjacent lithologies and thermal anomalies (Bruhn et al., 1994; Andrews et al., 1996; Lampe and Person, 2000). Besides the buoyancy-driven force, pore pressure gradients or lateral regional flow (LRF) from topography, magmatic, or metamorphic fluid production also cause hydrothermal activities (e.g. controlling the fluid flow and



heat transfer) (Wisian and Blackwell, 2004b), while the two flow modes may also coexist (McKenna and Blackwell, 2004b).
40 Several studies further reveal that these flow modes generate complex flow patterns within the faults (i.e., convection cells)
and/or across the adjacent permeable lithologies (Magri et al., 2016).

Transport mechanisms of hydrothermal convection in faulted zones, including preferential fluid flow pathways, dominant
heat transfer types (i.e., conduction, advection, and convection), and the mutual interactions of different flow modes, are crucial
for interpreting related diagenetic, petrophysical, and thermal phenomena in sedimentary basins. Therefore, it is necessary to
45 understand the transport mechanisms of hydrothermal convection in faulted zones, which are mainly controlled by the
permeability distributions of the fault systems and the surrounding lithologies, pore pressure gradients, and LRF (López and
Smith, 1995; Fairley, 2009). The dominant heat transfer types are quantified by analyzing the Peclet number, which in this
case represents the ratio of heat transfer by convection/advection to heat transfer by conduction (Jobmann and Clauser, 1994).
For Peclet numbers much less than 1 (e.g., < 0.1), the system is conduction-dominated, while for values greater than 1 the
50 system is convection/advection-dominated (Kämmlein et al., 2019). A Peclet number within the range of 0.1 and 1 indicates a
convective-conductive system (Beck et al., 1989). Furthermore, rock heterogeneities (e.g. anisotropic and depth-dependent
permeabilities), mainly resulting from sedimentary depositional environments, superimposed tectonics, and lithostatic stress,
are common phenomena in sedimentary basins (Parry, 1998; Achtziger-Zupančič et al., 2017a; Panja et al., 2021). Affected by
the preferential orientation of pore connectivity during deformation, the orientation of maximum permeability of faulted zones
55 commonly lies parallel to the fault plane (i.e., parallel to bedding) (Scibek, 2020). The horizontal permeability of sedimentary
rocks generally shows higher values than the vertical (i.e., perpendicular to bedding) permeability due to the effect of bedding,
as controlled by the sedimentary depositional environments (Panja et al., 2021). Permeability is generally expected to decrease
with increasing lithostatic pressure (Manning and Ingebritsen, 1999; Saar and Manga, 2004). Anisotropic and depth-dependent
permeabilities may change the fluid flow pathways and affect heat transfer (Guillou-Frottier et al., 2020). López and Smith
60 (1995) and Magri et al. (2016) presented 3D numerical investigations involving topography-driven flow and buoyancy-driven
flow to infer the transport mechanisms of a hydrothermal convection system. Magri et al.' hydraulic conditions were isotropic
and homogeneous, whereas López and Smith's simulation set partly anisotropic and heterogeneous hydraulic conditions. The
effects of thermo-hydraulic conditions, including permeability distributions of fault systems and surrounding lithologies, and
LRF, on the transport mechanisms, have not yet been systematically investigated.

65 A blueprint for complex hydrothermal conditions is the Piesberg Quarry, exposing Upper Carboniferous sandstones in
the Lower Saxony Basin (LSB) in northwestern Germany. The quarry is chosen as a reservoir analog because of its similarity
to still producing tight sandstone reservoirs in LSB concerning sedimentology, stratigraphy, fault patterns, and average
porosity. Tight sandstone, generally referred to low permeability reservoirs that produce mainly dry natural gas, is a common
play type of petroleum reservoir (Becker et al., 2019). This Upper Carboniferous sandstone quarry was affected by a kilometer-
70 scale thermal anomaly (270 ~ 300 °C), as interpreted from geothermometry data including fluid inclusion, K/Ar-dating,
chlorite thermometry, and vitrinite reflectance analyses (Wüstefeld et al., 2017b). Furthermore, the Piesberg Quarry is also an
experimental study case for the thermal control of a porosity-permeability evolution defined by long-term history matching in
this play type (Becker et al., 2019). Thus, revealing the transport mechanisms of the hydrothermal convection system in the
Piesberg Quarry is an effective strategy for interpreting related geological phenomena such as kilometer-scale thermal
75 anomalies).

Our study aims to systematically identify the transport mechanisms as inferred from the results of fluid flow and heat
transfer in the tight sandstone reservoir. For the first time, the example of the Upper Carboniferous Piesberg Quarry and its
geological past is used to numerically investigate the physical processes leading to the kilometer-scale thermal anomaly in
faulted tight sandstones. A 3D model is established based on the geological conditions of the Piesberg Quarry. Firstly,
80 considering complex thermo-hydraulic conditions, numerical modeling is performed, and the influence of the different
transport mechanisms is quantified. Then, the transport mechanisms are further assessed and discussed to study the effects of



the anisotropic and depth-dependent permeabilities on the transport mechanisms. Possible reasons for the kilometer-scale thermal anomaly in the Piesberg Quarry are inferred. Based on the generalized structural characteristics of the studied domain, the numerical results can be applied to interpret hydrothermal convection-related geological phenomena and to draw implications for future exploration and exploitation of reservoirs in analogous settings.

2 Material and Methods

2.1 The reservoir analog study area

The studied Piesberg Quarry is located at the southwestern margin of the LSB (Fig. 1a). The reservoir-scale Piesberg study site has dimensions of approximately 1 km in the W-E direction and 0.5 km in the N-S direction, with a depth of roughly 0.1 km (Fig. 1b).

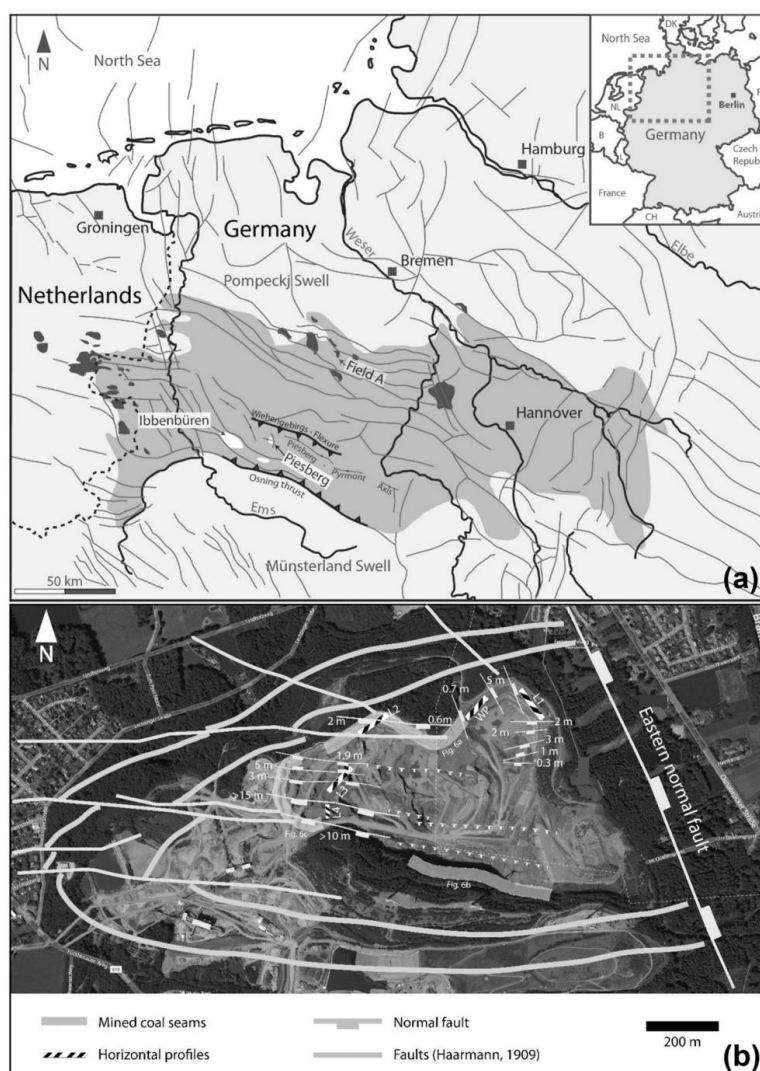


Figure 1. (a) Carboniferous outcrops (white in the dark grey area) at the southern rim of the LSB (dark grey area, after Senglaub et al. (2006)). The fault pattern of the LSB is based on Baldschuhn and Kockel (2000) and is extended with fault data from Kombrink et al. (2010). Black areas represent subsurface Carboniferous gas fields. (b) Aerial image of the Piesberg Quarry (© Microsoft, 2015). The coal seams, faults, and the main normal fault in the east are based on historical subsurface mining data (Haarmann, 1909). In addition, normal faults with dip direction indicators were observed within this study (Wüstefeld et al., 2017b).



Within the Piesberg Quarry, two dominant fault systems can be distinguished (Fig. 1a). First, the NNW-SSE striking normal fault (at $\sim 170^\circ$ strike angle) is represented in the east of the quarry (not exposed anymore), with a down-dip displacement of up to 600 m (Hinze, 1979; Bundesanstalt für Geowissenschaften und Rohstoffe, 2001; Baldschuhn et al., 2001). The second main strike orientation of the normal faults is W-E (at $\sim 95^\circ$ strike angle) to WNW-ESE, with average fault displacements of 10 m (Wuestefeld et al., 2014; Wüstefeld et al., 2017a; Becker et al., 2019). The initial total thickness of Upper Carboniferous sandstones in the region was 1.5 km (David et al., 1990). During the burial, the thickness of the sandstones decreased to nearly 1 km in the Late Jurassic to Early Cretaceous times. The sandstones are overlain by impermeable claystone and Zechstein cap rocks (Becker et al., 2019).

The geothermometry data from the outcrop samples in the Piesberg Quarry show a high-temperature thermal overprint of about $270 \sim 300^\circ\text{C}$ at about 4.4 km depth around the significant NNW-SSE striking normal fault at about 160 Ma. The NNW-SSE striking normal fault may thus have acted as a conduit for the heat/fluid source of the thermal overprint. Wüstefeld et al. (2017b) concluded that the local thermal increase of approximately $90 \sim 120^\circ\text{C}$ was the result of hydrothermal fluids circulating along the fault damage zone of the NNW-SSE striking normal fault, which laterally heated the tight sandstones. Furthermore, it is noteworthy that the W-E striking faults within the tight sandstones may also affect fluid flow and heat transfer processes because of their higher permeability (i.e., 10^{-13} m^2) and intersection with the NNW-SSE striking fault. Considering the geological conditions, especially fault patterns and stratigraphy, the Piesberg Quarry area might be an example of the coexistence of buoyancy-driven convective and lateral regional flows. Thermo-hydraulic numerical simulations are required to investigate and quantify the plausibility of different hypotheses of transport mechanisms that could contribute to the kilometer-scale thermal anomaly.

2.2 Numerical workflow

2.2.1 Governing equations

Inspired by the Piesberg Quarry, an idealized and synthetic numerical analog is created to characterize geological conditions in faulted tight sandstones and to enable investigation of the transport mechanisms leading to fluid flow and heat transfer. The numerical simulations for coupled fluid flow and heat transfer processes are carried out with a finite element open-source application called TIGER (THMC sImulator for GEoscience Research) (Gholami Korzani et al., 2019; Egert et al., 2020; Egert et al., 2021), which is based on the MOOSE (Multiphysics Object-Oriented Simulation Environment) framework (Permann et al., 2020). TIGER has been developed to tackle thermo-hydraulic-mechanical-chemical problems in petroleum and geothermal reservoirs. The numerical study of thermal convection in permeable and porous media involves coupling fluid flow and heat transfer equations as shown below (Gholami Korzani et al., 2020). The mass transport equation is written as

$$S_m \frac{\partial p}{\partial t} + \nabla \cdot \mathbf{q}_m = 0 \quad (1)$$

where S_m is the constrained specific storage of the porous media (Pa^{-1}), and p is the pore pressure (Pa). And the Darcy velocity is given as

$$\mathbf{q}_m = \frac{k}{\mu} (-\nabla p + \rho^l \mathbf{g}) \quad (2)$$

where μ is the dynamic fluid viscosity (Pa s), and \mathbf{g} is the gravitational acceleration vector ($\text{m}\cdot\text{s}^{-2}$).

The heat transfer equation is written as

$$\rho c_p \frac{\partial T}{\partial t} + \nabla \cdot (-\lambda \nabla T + \rho^l c_p^l \mathbf{q}_m) = 0 \quad (3)$$

where ρ is the effective density of porous media ($\text{kg}\cdot\text{m}^{-3}$), c_p is the effective specific heat capacity of porous media ($\text{J}\cdot\text{kg}^{-1}\cdot\text{K}^{-1}$), T is the temperature (K), t is the time (s), λ is the effective heat conductivity tensor of porous media, ρ^l is the density ($\text{kg}\cdot\text{m}^{-3}$) of fluid, c_p^l is the specific heat capacity ($\text{J}\cdot\text{kg}^{-1}\cdot\text{K}^{-1}$) of fluid, and \mathbf{q}_m is the Darcy velocity in the porous media ($\text{m}\cdot\text{s}^{-1}$).



2.2.2 Numerical model

The numerical model represents the stratigraphic distributions of the Piesberg Quarry region (belonging to the sandstone reservoir) at about 160 Ma. The model geometry extends 5 km along the W-E direction (i.e., X-axis), 12 km along the N-S direction (i.e., Y-axis), and over a depth of 12 km (i.e., Z-axis). The NNW-SSE striking fault (“main fault” in Fig. 2a) has a damage zone width of 400 m based on damage zone scaling relations to the fault displacement (Shipton et al., 2006; Torabi and Berg, 2011), a length of 12 km, and a height of 7 km (ranging from -11 km to -4 km on the Z-axis (Schultz et al., 2006)). In addition, three W-E striking faults (“transfer faults”) with 10 m width (along Y-axis) and 100 m height (along Z-axis) are embedded in the sandstone (Fig. 2b). To the west of the main fault, the sandstone is located at 3.9 ~ 4.9 km depth; to the east of the main fault, it is located at 4.5 ~ 5.5 km depth due to the 600 m displacement of the main fault. Lithologies that have similar permeability and heat conductivity are merged into a single lithological unit. Basement layers mainly consist of shale, limestone, and sandstone. The claystone and Zechstein are lumped into caprock at the top of the model. The model consists of 174,675 nodes connecting 827,610 tetrahedra, with mesh sizes of 1000 m for low permeability zones and mesh sizes of 100 m for high permeability zones. Preliminary mesh sensitivity analyses were performed to avoid any mesh dependency on the results.

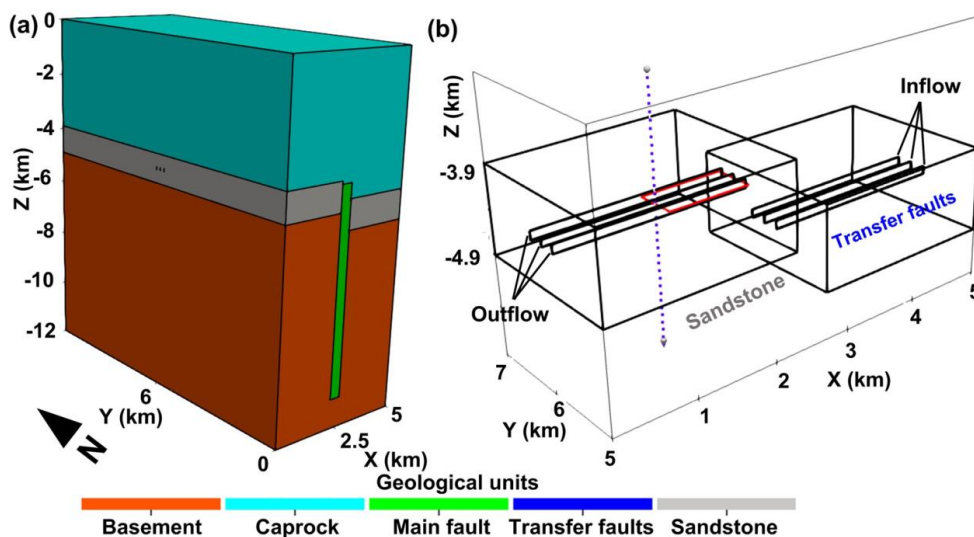


Figure 2. Model geometry of (a) the total model; (b) transfer faults embedded in the sandstone. The red rectangle, which is perpendicular to the main fault, represents the outline of the Piesberg Quarry. The dashed purple line shown in (b) is used to illustrate the extent of the temperature-depth profile.

The physical properties of each lithological unit are summarized in Table 1. The typical parameterization of main fault permeability (κ_{MF}) and sandstone permeability (κ_{SST}) are 10^{-13} m^2 and 10^{-15} m^2 , respectively. The transfer faults permeability (κ_{TF}) is constant at 10^{-13} m^2 . The fluid properties, including the temperature/pressure-dependent fluid density and dynamic viscosity, follow the NIST Chemistry Webbook (Linstrom and Mallard, 2001) and Smith and Chapman (1983). The boundary and initial conditions are set as follows. An air surface pore pressure of 10^5 Pa is fixed at the top of the model as a Dirichlet boundary condition. The initial condition of the hydraulic field corresponds to a hydrostatic gradient. The lateral sides of the model are assigned to no-flow boundary conditions in terms of pore pressure and temperature. The temperature at the top of the model is fixed at $20 \text{ }^\circ\text{C}$ as a Dirichlet boundary condition. A basal heat flux (BHF) of $0.1 \text{ W}\cdot\text{m}^{-2}$ represents the sum of the mantle heat flow and the heat emitted by the decay of radioactive elements in the crust (Wisian and Blackwell, 2004b), and is set at the bottom of the model as a Neumann boundary condition. The initial condition of the thermal field is derived from the steady-state simulation of heat conduction to avoid the effects of initial temperature perturbation on mass transport and heat transfer. Under the coexistence of buoyancy-driven convection, lateral convection, and LRF, Neumann boundary conditions



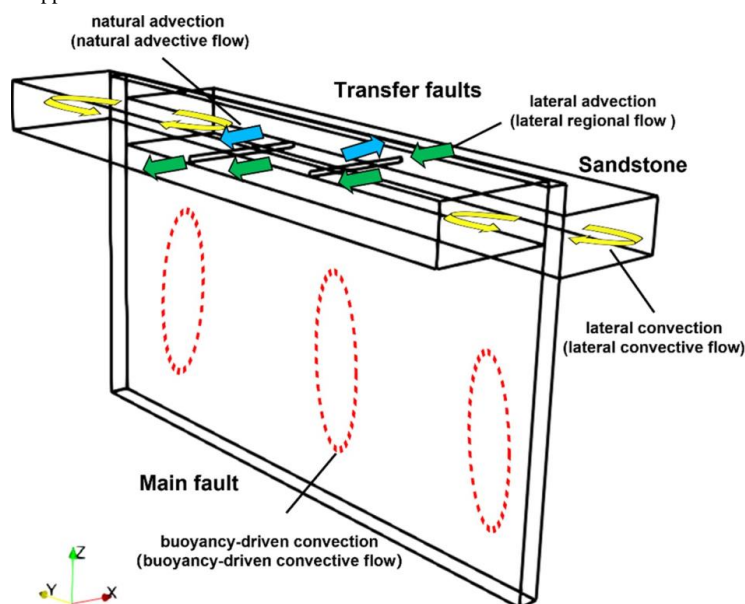
are superimposed on the eastern (as “inflow zones”) and western (as “outflow zones”) boundaries of the transfer faults, respectively (Fig. 2b). Surface elevations are not considered. The transient simulations are run up to 1 Myr, which allows the simulations to reach an approximate thermo-hydraulic equilibrium to compare the results of different transport mechanisms of hydrothermal convection.

170 **Table 1.** Parameters of the lithological units (Bruns et al., 2013; Wüstefeld et al., 2017a; Becker et al., 2019; Busch et al., 2019).

Properties	Caprock	Main Fault	Sandstone	Transfer faults	Basement
Porosity (-)	0.01	0.26	0.07	0.26	0.01
Compressibility (Pa ⁻¹)	10 ⁻¹⁰	10 ⁻¹⁰	10 ⁻¹⁰	10 ⁻¹⁰	10 ⁻¹⁰
Permeability (m ²)	5 · 10 ⁻¹⁸	10 ⁻¹⁵ ~ 10 ⁻¹³	10 ⁻¹⁶ ~ 10 ⁻¹⁴	10 ⁻¹³	10 ⁻²⁰
Density (kg m ⁻³)	1800	2000	2642	2000	2650
Specific heat capacity (J kg ⁻¹ K ⁻¹)	1000	1000	1000	1000	1000
Heat conductivity (W m ⁻¹ K ⁻¹)	3	2	2.5	2	2

2.3 Simulation cases

Based on the permeability distributions in the reservoir and LRF boundary conditions, the following simulations have been carried out to identify the different fluid flow pathways (Fig. 3) and to understand how the reservoir parametrization impacts fluid flow and heat transport. Buoyancy-driven convection in the main fault (Fig. 3, red dashed ovals) is triggered when its
 175 Rayleigh number exceeds the critical Rayleigh number 61 derived from the geometry of the main fault in Fig. 2. (Nield and Bejan, 2017). A benchmark test has been successfully carried out to reproduce the published results of Malkovsky and Magri (2016). Lateral convection in the sandstone (Fig. 3, yellow arrows) can be enhanced if the pore pressure difference between the sandstone and the main fault decreases (McKenna and Blackwell, 2004a). Natural advective flow in the transfer faults (Fig. 3, blue vectors) is getting significant when the transfer fault is more permeable than the main fault (Tzoufka et al., 2018). Apart
 180 from the natural advective flow, forced advection in the transfer faults (Fig. 3, green vectors) gets significant if an LRF boundary condition is applied.



185 **Figure 3.** Schematic representation of the modeled 3D main fault. Four different types of fluid flow pathways involving the lithological units are illustrated. The 3D main fault account for the relative displacement (i.e., 600 m) of the surrounding lithological units. Only one transfer fault is shown on both sides of the main fault for simplicity.

Herein, a reference case with typical play type parameterization (Table 1) has been selected to demonstrate the general behavior of fluid flow pathways and heat transfer types in the hydrothermal convection system. Then a sensitivity analysis is



conducted on the κ_{MF} (ranging from 10^{-15} m^2 to 10^{-13} m^2) and κ_{SST} (between 10^{-16} m^2 and 10^{-14} m^2) to identify their effects on the preferential fluid flow pathways and dominant heat transfer types. Then, these above-described permeability cases are superimposed by three representative LRFs. The LRFs range from $10^{-8} \text{ m}\cdot\text{s}^{-1}$ to $5 \cdot 10^{-7} \text{ m}\cdot\text{s}^{-1}$ (LRF_{max}). Besides the preferential fluid flow pathways and heat transfer types, the mutual interactions between the LRF and convective/advective flows are studied.

Furthermore, the effects of anisotropic and depth-dependent permeabilities on the transport mechanism are discussed. Many researchers show that the degree of permeability heterogeneity greatly varies even within the meter scale of the lithological unit (Ingebritsen and Manning, 1999; Saar and Manga, 2004). However, our discussion only focuses on the effects of the anisotropic and depth-dependent permeabilities of the main fault on the transport mechanisms. This is because the variation in lithostatic stress and sandstone properties is smaller than that of the main fault, and the low value of median κ_{SST} (i.e. 10^{-15} m^2). Farrell et al. (2014) shown the degree of anisotropy (i.e., horizontal permeability ($\kappa_{MF_vertical}$)/vertical permeability ($\kappa_{MF_horizontal}$)) of the fault ranges from one to three orders of magnitude. Thus, the $\kappa_{MF_horizontal}$ is set at one to three magnitudes (i.e., $10^{-16} \sim 10^{-14} \text{ m}^2$) lower than $\kappa_{MF_vertical}$ (i.e., 10^{-13} m^2), in which the anisotropic κ_{MF} is investigated. Influenced by the in situ lithostatic pressure distribution in the LSB (Manning and Ingebritsen, 1999; Saar and Manga, 2004), the κ_{MF} is exponentially decreased by one to three orders of magnitudes from its top locations (i.e., 10^{-13} m^2 at $z = -4 \text{ km}$ location) to its bottom locations (i.e., $10^{-16} \sim 10^{-14} \text{ m}^2$ at $z = -11 \text{ km}$ location). The above anisotropic and depth-dependent variations lie in the inferred ranges by Kuang and Jiao (2014) and Achtziger-Zupančič et al. (2017b).

In this study, the “thermal anomaly” is defined by the computed temperature minus the initial temperature distribution conditions. The maximum temperature at the western boundary of the Piesberg Quarry (T_{max}) is employed to compare with the geothermometer data. The temperature-depth profile following the western boundary of the Piesberg Quarry (Fig. 2b) and the median Peclet number of the lithological units are used to reveal the temperature distribution with depth and to identify the dominant heat transfer types, respectively. The median Peclet number of the main fault, transfer faults, and sandstone are abbreviated to Pe_{MF} , Pe_{TF} , and Pe_{SST} , respectively.

3 Results

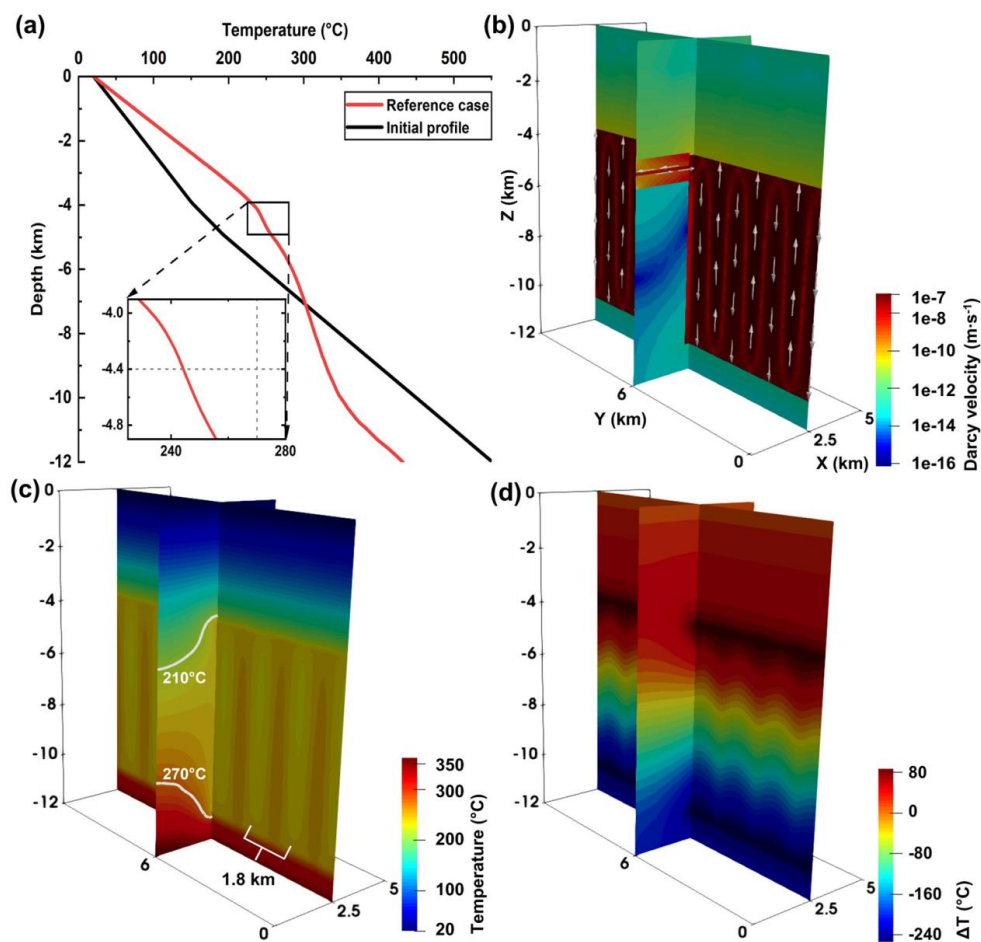
3.1 Reference case

A reference case is developed to demonstrate the general behavior of fluid flow pathways and heat transfer types in the hydrothermal convection system, as shown in Fig. 4. In the initial state ($t = 0 \text{ sec}$), the temperature and its gradient increase with depth depending on the thermal conductivities of deep lithological units (black line in Fig. 4a). At 1 Myr, the buoyancy-driven convection in the main fault with $Pe_{MF} = 9.0$ results in thirteen convective cells which consist of seven downflows and upflows in each at the maximum Darcy velocity of $1.1 \cdot 10^{-7} \text{ m}\cdot\text{s}^{-1}$ (Fig. 4b). The buoyancy-driven convection is triggered by fluid density variations resulting from the temperature difference. The mentioned upward and downward flows of fluids generate six full and one-half thermal plumes, as shown in Fig. 4c. The convective flow transports heat upwards inside the main fault. Thus, compared to the initial temperature distribution (black line in Fig. 4a), the buoyancy-driven convection results in positive thermal anomalies ranging between 0°C and 86°C in the shallow part of the main fault (i.e., $z = -6 \sim -4 \text{ km}$ locations in Fig. 4d).

Initiated by the same permeability of the main fault and transfer faults (i.e., 10^{-13} m^2), the lateral convection in the transfer faults with $Pe_{TF} = 0.5$ includes fluid recharge and discharge processes at the maximum Darcy velocity of $4.6 \cdot 10^{-8} \text{ m}\cdot\text{s}^{-1}$ as shown in Fig. 4b. The heated fluid recharges from the main fault into the shallow part of the transfer faults (i.e., $z = -4.4 \sim -4.35 \text{ km}$ locations) and discharges from the deep part of the transfer faults (i.e., $z = -4.45 \sim -4.4 \text{ km}$ locations) into the main fault, respectively. However, the temperature-depth profile of the reference case (i.e., the red line in Fig. 4a) shows that the lateral convection has a negligible effect on increasing the temperature in the transfer faults because of the



230 narrow (i.e., width 10 m) and thin (i.e., thickness 100 m) geometry conditions of the transfer faults and the low permeability
of the surrounding sandstone (i.e., 10^{-15} m^2).



235 **Figure 4.** Fluid flow and temperature fields of the reference case. (a) Temperature-depth profiles which follow the western boundary of the Piesberg Quarry (Fig. 2b) at the initial time and when T_{max} is reached, respectively. At 1 Myr, cross-sectional views of the (b) flow field with arrows representing the preferential fluid flow pathways; (c) resulting temperature distributions. The 210 °C and 270 °C isotherms are highlighted; (d) temperature differences compared to the initial conductive temperature distribution.

240 Figure 4b shows that the reference case yields weak fluid flow with Darcy velocity $\leq 5 \cdot 10^{-9} \text{ m} \cdot \text{s}^{-1}$ in the sandstone, caprock, and basement units (“off-faults domains”) owing to their relatively low permeabilities (i.e., $\leq 10^{-15} \text{ m}^2$). The temperature distribution in the off-fault domains (e.g., $Pe < 0.1$) is mainly dominated by heat conduction, as shown in Figs. 4a and 4c. Influenced by the thermal anomalies inside the main fault, heat conduction leads to upward-convex isotherms in the units located near the shallow region of the main fault (i.e., $z = -7.5 \sim -4 \text{ km}$ locations in Fig. 4c). However, heat conduction causes downward-convex isotherms in the units located near the deep region of the main fault (i.e., $z = -11 \sim -7.5 \text{ km}$ locations in Fig. 4c). The resulting upward- and downward-convex isotherms agree with an increase and decrease in temperature above and below 7 km depth (red line in Fig. 4a) compared to the initial temperature profile (black line in Fig. 4a), respectively. Additionally, impacted by the convective mass flow, a pore pressure perturbation ($\sim -2.8 \text{ MPa}$) around the main fault extends $\sim 0.3 \text{ km}$ in the sandstone and transfer faults at a depth of 4.4 km.

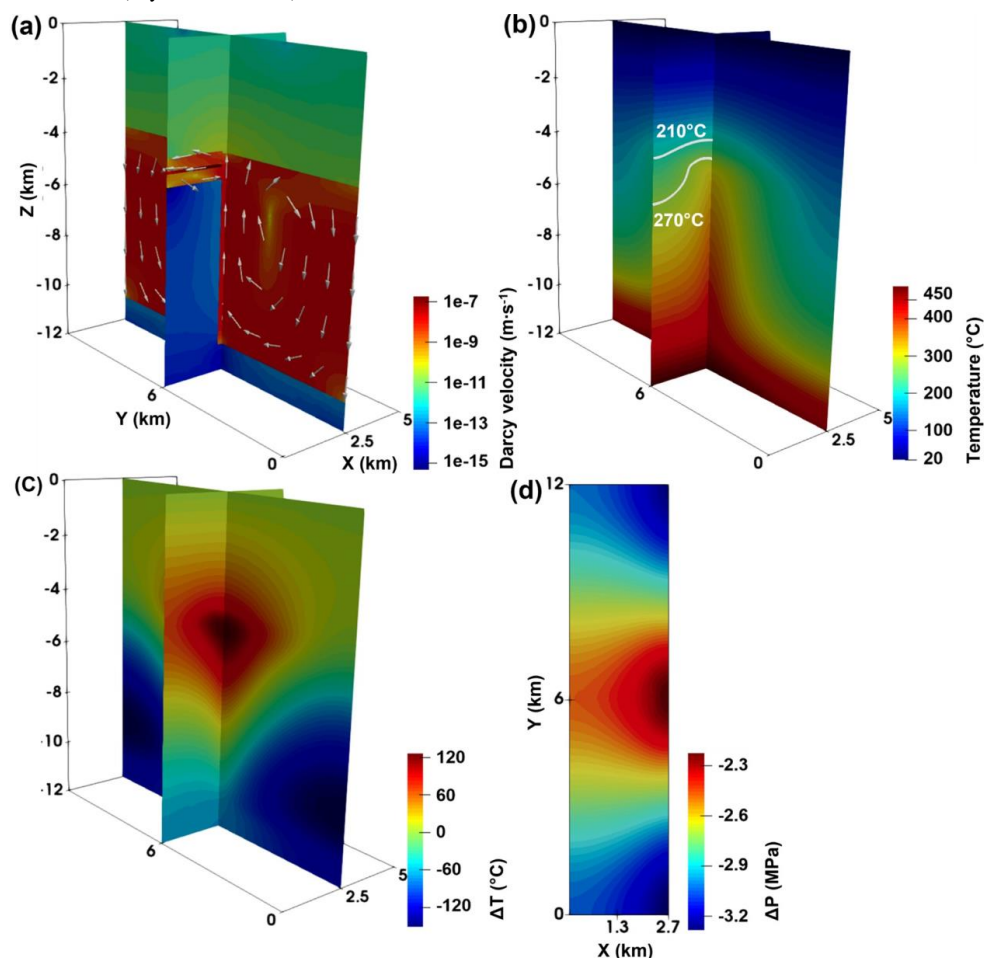
245



3.2 Effects of permeability distributions

3.2.1 Main fault

We evaluate how the κ_{MF} variations affect the fluid flow pathways and heat transfer types in the hydrothermal convection system. Their differences compared to the reference case are described as follows. The $\kappa_{MF} = 10^{-14} \text{ m}^2$ case results in eight buoyancy-convection cells in the main fault with $Pe_{MF} = 2.6$ and three times lower maximum Darcy velocity of the convective flow than in the reference case with $\kappa_{MF} = 10^{-13} \text{ m}^2$. In addition to the above differences, the $\kappa_{MF} = 10^{-14} \text{ m}^2$ case has a similar focused flow in the faults and conduction-dominated heat transfer in the sandstone to the reference case. Results of fluid flow, temperature, and pore pressure change 1 Myr are illustrated in Fig. 5. for the $\kappa_{MF} = 10^{-15} \text{ m}^2$ case. It is observed in Fig. 5a that the $\kappa_{MF} = 10^{-15} \text{ m}^2$ case leads to two buoyancy-driven convection cells in the main fault with $Pe_{MF} = 0.7$ and eight times lower maximum Darcy velocity of the convective flow than in the reference case. Figures 5b and 5c show that the temperature increases in the center of the main fault ($\sim y = 6 \text{ km}$), associated with the upward flow of fluid, and decreases along the main fault's lateral sides ($\sim y = 0$ and 12 km).

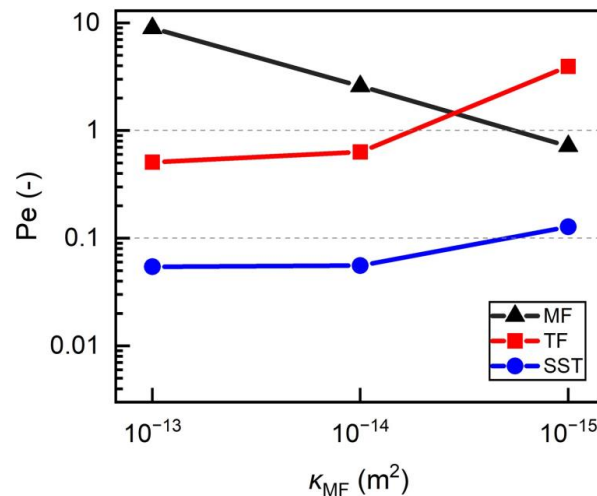


260 **Figure 5.** Fluid flow, temperature, and pore pressure change fields of the $\kappa_{MF} = 10^{-15} \text{ m}^2$ case at 1 Myr. Cross-sectional view of the (a) flow field with arrows representing the preferential fluid flow pathways; (b) resulting temperature field. The 210 °C and 270 °C are highlighted; (c) temperature differences compared to the initial conductive temperature distribution; (d) top view of the pore pressure change compared to the initial hydrostatic pressure (43.3 MPa) in the western sandstone, transfer faults, and main fault at a depth of 4.4 km. The 1.3 km and 2.7 km along the X-axis follow the west boundary of the Piesberg Quarry and the eastern boundary of the main fault, respectively.



From Fig. 5a, it is observed that the lateral convection can be enhanced in the sandstone, especially in the part (i.e.,
 265 $Pe_{SST} \geq 0.9$) near the main fault, by the equal κ_{MF} and κ_{SST} (i.e., 10^{-15} m^2). The lateral convection consists of fluid recharge
 and discharge processes at a maximum Darcy velocity of $10^{-8} \text{ m} \cdot \text{s}^{-1}$, slightly lower than the buoyancy-driven convection. The
 heated fluid recharges from the central part of the main fault into the sandstone and discharges from the sandstone into the
 main fault's margins, respectively. Furthermore, caused by the large permeability contrast between the transfer faults and the
 main fault (i.e., $\kappa_{TF}/\kappa_{MF} = 100$), the natural advective flow in the transfer faults with $Pe_{TF} = 3.9$ propagates towards the lateral
 270 boundaries of the model as shown in Fig. 5a. The maximum Darcy velocity of the natural advective flow reaches $1.7 \cdot 10^{-7} \text{ m} \cdot \text{s}^{-1}$,
 which is one order higher than the buoyancy-driven convection. Figures 5b and 5c demonstrate that, compared to the
 reference case, the increased mass flow involved in the lateral convection and natural advection effectively causes elevated
 temperatures in the sandstone and transfer faults near the center of the main fault. Affected by the increased mass flow, the
 convective/advective flow processes in the main fault, sandstone, and transfer faults result in a larger ($\sim 3.2 \text{ MPa}$) and more
 275 extensive ($0 \sim 5 \text{ km}$) pore pressure perturbation than in the reference case as shown in Fig. 5d.

In the following, we study how κ_{MF} variations affect the dominant heat transfer types and temperature distribution with
 depth. With the κ_{MF} decreased from 10^{-13} m^2 to 10^{-15} m^2 , the number of convection cells is reduced from thirteen to two, and
 the maximum Darcy velocity of the buoyancy-driven convective flow is decreased from $1.1 \cdot 10^{-7} \text{ m} \cdot \text{s}^{-1}$ to $1.4 \cdot 10^{-8} \text{ m} \cdot \text{s}^{-1}$
 (Figs. 4b and 5b). These variations show that the intensity of the buoyancy-driven convection within the main fault becomes
 280 relatively weak and correspondingly, the Pe_{MF} is also decreased from 9.0 to 0.7 as shown in Fig. 6. Thus, the upward energy
 transfer by the buoyancy-driven convection within the main fault is reduced. Conversely, the energy stored at the bottom of
 the model increases as the κ_{MF} is decreased. This is illustrated by the increase in bottom temperature from $432 \text{ }^\circ\text{C}$ to $519 \text{ }^\circ\text{C}$,
 as shown in Fig. 7.

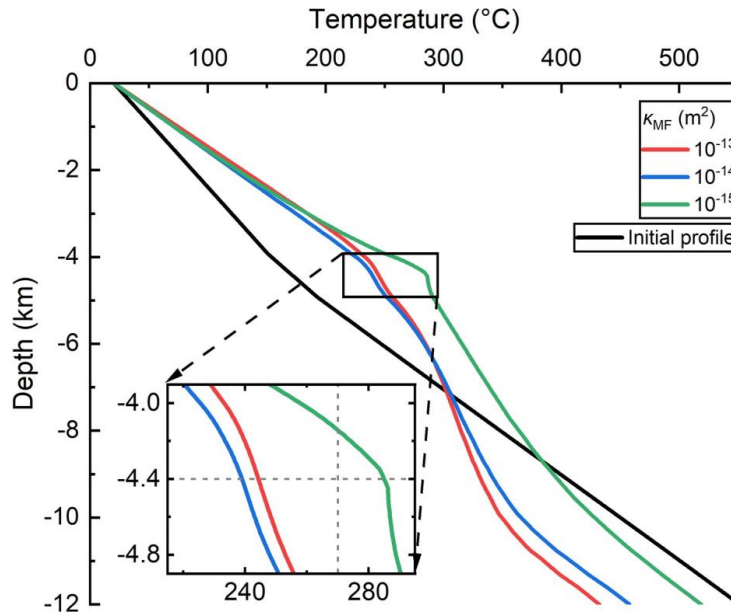


285 **Figure 6.** Effects of the main fault permeability (κ_{MF}) on the Pe (median Peclet numbers) of the main fault (MF), transfer faults (TF), and sandstone (SST).

Figure 6 shows that for the $\kappa_{MF} = 10^{-14} \text{ m}^2$ case, fluid flow is mainly confined in the faults and the heat transfer is
 dominated by conduction in the sandstone with $Pe_{SST} < 0.1$, in agreement with the reference case. Thus, the energy conducted
 from the main fault and basement into the sandstone is decreased when the κ_{MF} is reduced from 10^{-13} m^2 to 10^{-14} m^2 . This is
 290 evidenced by the decrease in T_{max} from $244 \text{ }^\circ\text{C}$ to $239 \text{ }^\circ\text{C}$ as shown by their temperature-depth profiles (i.e., the red and blue
 lines in Fig. 7). The $\kappa_{MF} = 10^{-15} \text{ m}^2$ case (i.e., the green line in Fig. 7) results in higher temperature in the range of $z = -12 \sim -$
 3.5 km than the other two cases. This is due to the larger depth extent (i.e., $z = -9 \sim -4 \text{ km}$ locations) and maximum magnitude
 (i.e., $130 \text{ }^\circ\text{C}$) of the positive thermal anomaly (Fig. 4d) near the central part of the main fault compared to the reference case
 (Fig. 5c). Furthermore, in the case with $\kappa_{MF} = 10^{-15} \text{ m}^2$, the upward energy transfer within the main fault is less than in the other



295 two cases (i.e., $\kappa_{MF} = 10^{-13} \text{ m}^2$ and 10^{-14} m^2 cases). However, the enhanced lateral convection and natural advection efficiently increase the fluid and heat flows from the main fault to the sandstone (with $Pe_{SST} = 0.13$) and transfer faults (with $Pe_{TF} = 3.9$), higher than the conduction-dominated heat transfer. Consequently, the temperature increases significantly in the sandstone range of $z = -4.9 \sim -3.9 \text{ km}$ as shown by its temperature-depth profile (blue line in Fig. 7), unlike in the other two cases. $\kappa_{MF} = 10^{-15} \text{ m}^2$ results in a higher T_{max} of $285 \text{ }^\circ\text{C}$ (green line in Fig. 7), which is $41 \text{ }^\circ\text{C}$ higher than the reference case.



300

Figure 7. Effects of the main fault permeability (κ_{MF}) on the temperature-depth profiles. The $\kappa_{MF} = 10^{-13} \text{ m}^2$ case represents the reference case.

3.2.2 Sandstone

We investigate the effects of the κ_{SST} variations on the transport mechanisms of the hydrothermal convection system. The $\kappa_{SST} = 10^{-16} \text{ m}^2$ case results in eleven buoyancy-convection cells in the main fault with $Pe_{MF} = 9.1$ and a similar maximum Darcy velocity of the convective flow to the reference case with $\kappa_{SST} = 10^{-15} \text{ m}^2$. It has a similar concentrated flow in the faults and conduction-dominated heat transfer in the sandstone to the reference case. Results of fluid flow, temperature, and pore pressure change at 1 Myr are shown in Fig. 8 for the $\kappa_{SST} = 10^{-14} \text{ m}^2$ case. Focusing on Fig. 8b, it is observed in the $\kappa_{MF} = 10^{-14} \text{ m}^2$ case leads to fourteen convective cells in the main fault with $Pe_{MF} = 8.3$ and similar maximum Darcy velocity of the convective flow to the reference case due to their nearly same Pe_{MF} (Fig. 9).

310

Initiated by the high κ_{MF} and κ_{TF} , the lateral convection in the sandstone (i.e., $Pe_{SST} = 0.5$) and transfer faults (i.e., $Pe_{TF} = 1.0$) is limited and consists of fluid recharge and discharge processes as shown in Fig. 8a. The heated fluid recharges from the main fault into the shallow part (i.e., $z = -4.4 \sim -3.9 \text{ km}$ locations) of the sandstone and transfer faults and discharges from the deep part (i.e., $z = -4.9 \sim -4.4 \text{ km}$ locations) of the sandstone and transfer faults into the main fault, respectively. The maximum Darcy velocity of the recharge and discharge processes reaches $4.6 \cdot 10^{-8} \text{ m} \cdot \text{s}^{-1}$, which is ten times higher than in the reference case (Fig. 8a). Figures 8b and 8c show that the increased mass flow involved in the lateral convection raises the temperature in the sandstone and transfer faults compared to the reference case. The isotherms of mixed concave-convex shapes in the sandstone range demonstrate that the lateral convection results in a higher temperature rise in the shallow part than the deep part of the sandstone and transfer faults. This is due to the energy and fluid losses in the discharge process. From Fig. 8d, it is observed that the lateral convection causes larger ($\sim -2.9 \text{ MPa}$) and more extensive ($\sim 1.8 \text{ km}$) pore pressure disturbances in the sandstone and transfer faults at a depth of 4.4 km than in the reference case.

320

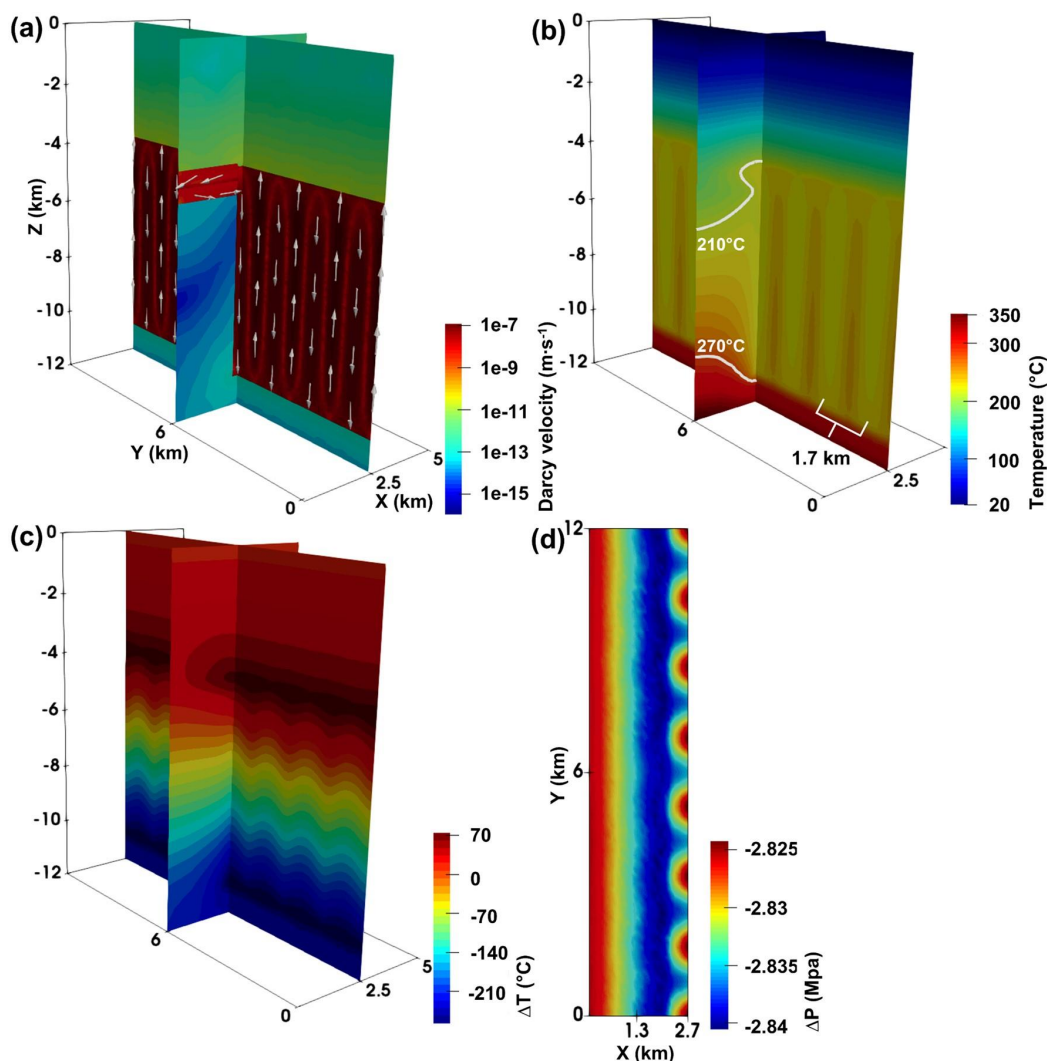


Figure 8. Fluid flow, temperature, and pore pressure change fields of the $\kappa_{SST} = 10^{-14}$ case at 1 Myr. Cross-sectional view of the (a) flow field with arrows representing the preferential fluid flow pathways; (b) resulting temperature field. The 210 °C and 270 °C isotherms are highlighted; (c) temperature differences compared to the initial hydrostatic pressure (43.3 MPa) in the western sandstone, transfer faults, and main fault at a depth of 4.4 km. The 1.3 km and 2.7 km along the X-axis follow the west boundary of the Piesberg Quarry and the eastern boundary of the main fault, respectively.

Next, we illustrate how the κ_{SST} variations affect the dominant heat transfer types and temperature distribution with depth. With the κ_{SST} increased from 10^{-16} m^2 to 10^{-14} m^2 , the lateral convection in the sandstone and transfer faults is gradually enhanced which is evidenced by the increased Pe_{SST} from ~ 0 to 0.5 (Fig. 9). This is caused by the reduced pore pressure difference between the main fault and the sandstone due to their decreased permeability contrasts.

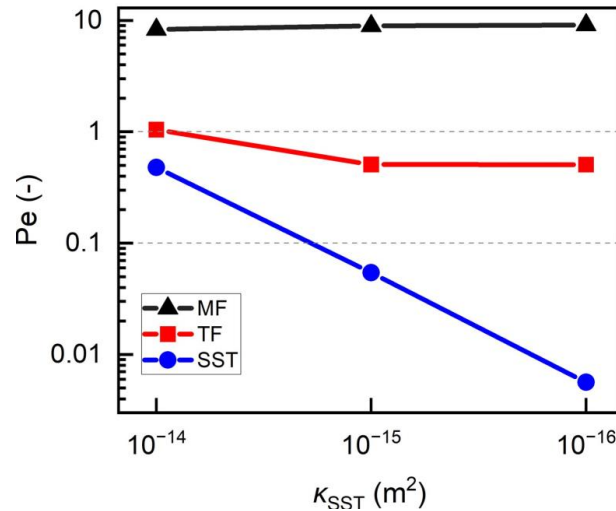


Figure 9. Effects of the sandstone permeability (κ_{SST}) on the Pe (median Peclet numbers) of the main fault (MF), transfer faults (TF), and sandstone (SST).

335 Figure 10 illustrates divergent temperature distributions within the 2 km to 5 km depth for all three κ_{SST} cases. The $\kappa_{SST} = 10^{-16} m^2$ case yields a continuous rise of temperature down to 5 km depth due to conduction-dominated heat transfer in the sandstone ($Pe_{SST} \approx 0$) as shown by its temperature-depth profile (i.e., the green line in Fig. 10). A slightly decreased T_{max} (i.e., 244 °C) is observed in the reference case (Fig. 10, red line) compared to the $\kappa_{SST} = 10^{-16} m^2$ case (i.e., 248 °C) (Fig. 10, green line). The reason is that weak lateral convection ($Pe_{SST} = 0.1$) transfers energy into the sandstone away from the main fault and decreases the temperature of the sandstone near the main fault. However, a higher temperature increase within the 2 km to 4.8 km depth is shown for the $\kappa_{SST} = 10^{-14} m^2$ case (Fig. 10, blue line). The T_{max} in the $\kappa_{SST} = 10^{-14} m^2$ case is 269 °C, which is 25 °C higher than in the reference case. This is due to the increased mass flow involved in the enhanced lateral convection (i.e., $Pe_{SST} = 0.5$), which transfers the energy from the main fault into the sandstone, transfer faults, and caprock. The energy and fluid losses in the discharge process cause lower temperature rises than the recharge process in lateral convection. Compared to linear temperature distribution at the initial time, the mixed concave-convex shapes of the temperature profile (Fig. 10, blue line) agree with the isotherms and fluid flow pathways of the lateral convection within the sandstone (Figs. 8a and 8b).

340

345

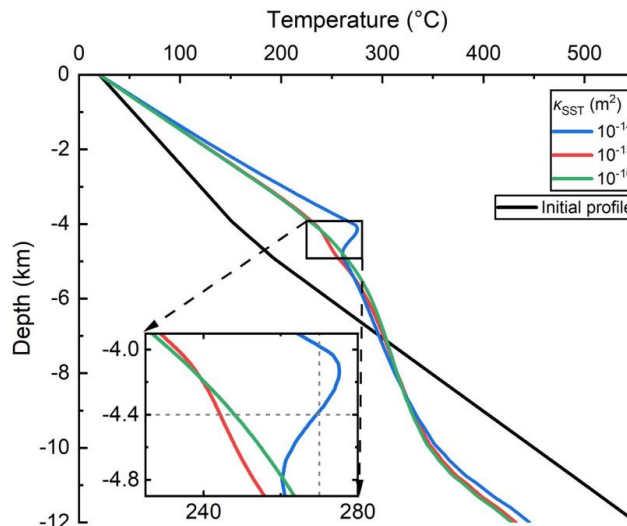


Figure 10. Effects of the sandstone permeability (κ_{SST}) on the temperature-depth profiles. The $\kappa_{SST} = 10^{-15} m^2$ case represents the reference case.

350



3.3 Effects of lateral regional flow

Here we study whether a superimposed LRF changes the fluid flow pathways and types of heat transfer in the hydrothermal convection system. The mutual interaction between LRF and convective/advective flows is also studied. The reference case superimposed by LRFs is used to investigate whether an LRF enhances heat extraction and transfer from the buoyancy-driven convection within the main fault. The results show that forced advection is initiated in the transfer faults only when the LRF exceeds the buoyancy-driven convective flow in the reference case. The dominant heat transfer type in the transfer faults changes from conduction to advection, as proven by the increased Pe_{SST} from 0.5 to 2.3 (Schilling et al., 2013). The LRF of $5 \cdot 10^{-7} \text{ m} \cdot \text{s}^{-1}$ superimposed on the reference case increases the T_{max} by 8 °C compared to the reference case without LRF (Table 2).

Table 2. The effect of maximum lateral regional flow ($LRF_{max}=5 \cdot 10^{-7} \text{ m} \cdot \text{s}^{-1}$) on the maximum temperature at the western boundary of the Piesberg Quarry (T_{max}) under different permeability distributions of the main fault (κ_{MF}) and sandstone (κ_{SST}).

Permeability distributions (m^2)	T_{max} (°C)		Effect of LRF_{max} on elevating the T_{max} (°C)	
	no LRF	superimposed by LRF_{max}		
κ_{MF}	10^{-13}	244	252	8
	10^{-14}	239	249	10
	10^{-15}	285	314	29
κ_{SST}	10^{-14}	269	271	2
	10^{-15}	244	252	8
	10^{-16}	248	261	13

The interactions between the LRF, buoyancy-driven convective flow, and natural advective flow are shown in the κ_{MF} variation cases in Table 2. As mentioned in Sect. 3.2.1, the maximum Darcy velocity of the buoyancy-driven convective flow is reduced when κ_{MF} is decreased from 10^{-13} m^2 to 10^{-15} m^2 . Therefore, the extent to which the LRF_{max} overwhelms the buoyancy-driven convective flow increases. This is evidenced by the increased Pe_{TF} ranging from 2.3 to 6.7. In contrast, the natural advective flow in the transfer faults gets significant when κ_{MF} is decreased to 10^{-15} m^2 . Figure 5a shows that the natural advective flow in the western part propagates towards the western boundaries of the model, which is the same as the LRF. Thus, the LRF_{max} can enhance the heat and mass flow in the transfer faults, leading to a larger increase in T_{max} (ranging from 8 °C to 29 °C) compared to the cases without LRF (Table 2).

The κ_{SST} variation cases in Table 2 illustrate the interactions between the LRF, buoyancy-driven convective flow, and lateral convective flow. Section 3.2.2 shows that the lateral convective flow is gradually weakened (Figs. 4b and 8a) when κ_{SST} is decreased from 10^{-14} m^2 to 10^{-16} m^2 . The maximum Darcy velocity of the buoyancy-driven convective flow is $\sim 1 \cdot 10^{-7} \text{ m} \cdot \text{s}^{-1}$, nearly the same in all κ_{SST} cases. Thus, the LRF_{max} can also enhance the heat and mass flows in the sandstone and transfer faults when the κ_{SST} is decreased, causing larger T_{max} (from 2 °C to 13 °C) (Table 2) and increased Pe_{TF} ranging from 2 to 5.4.

According to the above results, the impact of LRF on enhancing the mass and heat flows within the sandstone and transfer faults is reduced for higher κ_{MF} and κ_{SST} cases (López and Smith, 1996; Sheldon et al., 2012). The reason is that the higher κ_{MF} (i.e., 10^{-13} m^2) and κ_{SST} (i.e., 10^{-14} m^2) lead to a stronger fluid flow and heat transfer in the buoyancy-driven convection and lateral convection, respectively. Thus, the fluid mass fraction that can be impacted by LRF is decreased, resulting in less effect on the increased T_{max} compared to the lower κ_{MF} and κ_{SST} cases.

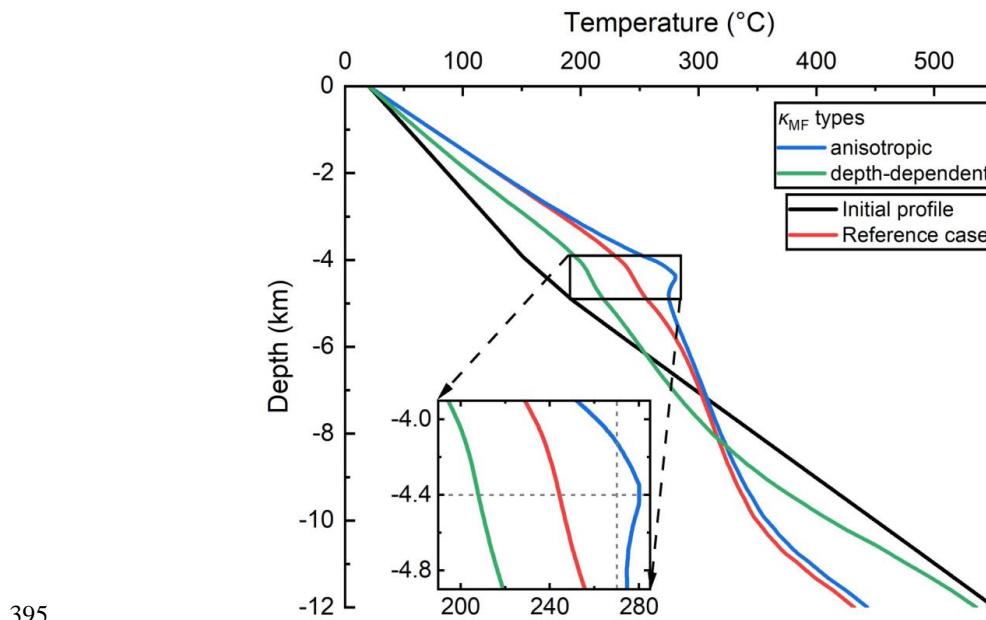
4 Discussions

4.1 Effects of the anisotropic and depth-dependent permeabilities

We consider the anisotropic κ_{MF} cases described in Sect. 2.3 to study how the anisotropic permeability affects the transport mechanisms. Preliminary tests show that the cases with the one and three orders degree of anisotropy in the κ_{MF} have similar concentrated flow in the faults and conduction-dominated heat transfer in the sandstone to the reference case. They result in a



390 T_{\max} of ~ 240 °C, which is 4 °C lower than the reference case. This suggests that the anisotropic main fault acts as a complex pipe-barrier system that favors vertical fluid migration and impedes horizontal fluid migration. In contrast, the κ_{MF} case with two orders of magnitude of anisotropy leads to an elevated temperature in the $z = -7 \sim -3$ km range, especially in the sandstone range of $z = -4.9 \sim -3.9$ km, as shown by its temperature-depth profile (i.e., the blue line in Fig. 11). The T_{\max} is elevated to 280 °C, which is 36 °C higher than in the reference case. This is caused by the enhanced lateral convection in the sandstone ($Pe_{SST} = 0.1$) and natural advection in the transfer faults ($Pe_{TF} = 4.6$) that transfer energy more efficiently than the conduction-dominated heat transfer. The lateral convection and natural advection are initiated by the decreased horizontal permeability contrast between the sandstone and main fault, and the increased horizontal permeability contrast between the transfer faults and main fault, respectively.



395

Figure 11. Effects of the anisotropic and depth-dependent permeabilities of the main fault (κ_{MF}) on the temperature-depth profiles.

The depth-dependent κ_{MF} cases are used to study depth-dependent permeability effects on transport mechanisms. All the depth-dependent κ_{MF} cases have similar focused flow in the faults and conduction-dominated heat transfer in the sandstone to the reference case. However, the number of upward flows within the main fault is decreased in all three cases. When the degree of depth-dependent κ_{MF} is reduced from one to three orders of magnitudes, the amount of upward transported energy by the buoyancy-driven convection within the main fault is gradually decreased, resulting in a decreased Pe_{MF} , ranging between 6.7 and 0.9. The T_{\max} is decreased from 217 °C to 195 °C with the decreased degree of depth-dependent κ_{MF} . Inferred from the in situ lithostatic pressure distribution in the LSB (Manning and Ingebritsen, 1999; Saar and Manga, 2004), the κ_{MF} is exponentially decreased by two orders of magnitudes from its top locations to its bottom locations. Its equation is shown as

405
$$\kappa_{MF}(z) = 10^{-13} \times e^{\frac{z+4000}{1520}} \quad (4)$$

where z is the location (m) and $\kappa_{MF}(z)$ is the main fault permeability (m^2) at the z (m) location. The resulting temperature profile is shown by its temperature-depth profile (i.e., the green line in Fig. 11) with a T_{\max} of 207 °C.

The anisotropic permeability cases prove that the onset of lateral convection and natural advection relies on the horizontal permeability contrast between the sandstone and main fault, and the horizontal permeability contrast between the transfer faults and main fault, respectively. Influenced by the increasing lithostatic pressure with depth, the mass flow and heat transfer of the buoyancy-driven convection is gradually weakened in the main fault. Thus, the main controlling parameter of the transport

410



mechanism is detailed from the idealized permeability distributions into the directional and spatial permeability distributions of the main fault and sandstone.

4.2 Implications for the kilometer-scale thermal anomaly in the Piesberg Quarry and comparable reservoirs

415 Our study performs the first evaluation of the effects of the geological conditions on generating the kilometer-scale thermal
anomaly (270 ~ 300 °C) in the Piesberg Quarry. Since only the geothermometry data from the outcrop samples in the Piesberg
Quarry are available, our discussion will be limited to the thermal profiles at 4.4 km depth where the Piesberg Quarry was
located during Late Jurassic-Early Cretaceous. The relation between temperatures and mass flows within the sandstone and
transfer faults (shown in Figs. 4, 5, and 8) suggests that the thermal anomaly results from buoyancy-driven convection in the
420 main fault, lateral convection in the sandstone, and advection in the transfer faults rather than from conduction-dominated heat
transfer. Within the coexisting modes in Fig. 5d, buoyancy-driven convection is an essential prerequisite for the formation of
high temperatures in relatively shallow depths as a positive anomaly (Bächler et al., 2003; Kohl et al., 2000). The main role
played by lateral convection and natural advection is to redistribute both heat and fluid mass within the lithological units
(McKenna and Blackwell, 2004a; Wisian and Blackwell, 2004a), as shown in Fig. 3 and the results obtained in Sect. 3.
425 Favorable permeability distributions for the onset of lateral convection in the sandstone and advection in the transfer faults
include moderately permeable sandstone (i.e., 10^{-14} m²), same permeabilities (i.e., 10^{-15} m²) in the main fault and sandstone,
and the anisotropic case of the main fault (i.e., $\kappa_{MF_vertical}/\kappa_{MF_horizontal} = 10^{-13}$ m²/10⁻¹⁵ m²). The T_{max} obtained from the
simulations for these three cases are 269 °C, 285 °C, and 280 °C, respectively. Wuestefeld et al. (2014) and Becker et al.
(2019) study the permeability heterogeneity properties in the Piesberg Quarry. Based on the in situ geological and petrophysical
430 properties (i.e., mean permeability distribution, heterogeneities) around Piesberg Quarry and within the LSB (Wuestefeld et
al., 2014; Wüstefeld et al., 2017a; Becker et al., 2019), the increased mass flows involved in the coexisting flow modes resulting
from the anisotropic case of the main fault, provide the most realistic permeability distribution case to explain the thermal
anomaly in the Piesberg Quarry.

In order to make geothermal projects more economically attractive, especially in sedimentary basins (e.g., LSB) with
435 constraint conditions (e.g., low permeability and temperature gradient), fractured/faulted zones are preferentially targeted as
valuable geothermal reservoirs (Bruns et al., 2013). As shown in the reference case (Fig. 4), the upward fluid flow within the
main fault leads to positive thermal anomalies (i.e., at a maximum of 86 °C) in a relatively shallow depth (~ 4 km). The
relatively shallow locations of geothermal reservoirs greatly decrease the investments (i.e., the costs of drilling and
completions) for developing geothermal energy in the sedimentary basin (Huenges and Ledru, 2010). The processes within
440 geothermal reservoirs have important consequences for their successful exploration since the interesting scale at which thermal
anomalies could be exploited greatly depend on the heat transfer types and fluid flow pathways (Huenges and Ledru, 2010;
Przybycin et al., 2017). If the temperature anomaly is assumed to persist to the present and geologic conditions are constant,
for the given reference case geothermal drilling should target the kilometer-scale elevated temperatures (i.e., 2.8 km on the x-
axis; 12 km on the y-axis; 2.8 km on the z-axis) around the depth of 4 km (Fig. 4). Our 3D numerical model allows for a better
445 understanding of the processes within geothermal reservoirs (e.g., the role of different selected parameters in the origin,
location, scale, and magnitude of thermal anomalies), thus providing tools for predicting and targeting geothermal exploration
(Clauser and Villinger, 1990; Guillou-Frottier et al., 2013).

5 Conclusions

Inspired by the Piesberg Quarry in Northern German and its established thermal anomaly, we created an idealized numerical
450 model to derive parameters and processes that cause the onset of thermal anomalies in comparable geological settings. The
study focused on the developments and mutual interactions of predominant heat transfer types and preferential fluid flow



pathways in faulted tight sandstones. The hydraulic parameterizations of the main fault and sandstone are crucial for inferring the mechanisms causing the transport of fluid and heat. Buoyancy-driven convection transports energy upward inside the main fault. Induced by favorable hydraulic conditions (e.g., high sandstone permeability of 10^{-14} m²; equal permeability of 10^{-15} m² of the main fault and sandstone), convective flow in the sandstone and advective flow in the transfer faults redistribute both heat and fluid within the reservoir, causing elevated temperatures (≥ 269 °C) and thermal gradients in the sandstones compared to conduction-dominated heat transfer (≤ 250 °C). Lateral regional flow can interact with convective/advective flows in the sandstone and transfer faults, and changes the dominant heat transfer from conduction to advection in the transfer faults when it overwhelms the magnitude of the convective flows in the main fault and sandstone. However, its influence is limited by the geometric and hydraulic constraints of the transfer faults and, therefore, significantly reduced compared to the influence of the local permeability distribution. The anisotropic and depth-dependent permeability cases detail the main controlling parameter of the transport mechanism into the directional and spatial permeability distributions of the main fault and sandstone.

The increased mass flows involved in the coexisting flow modes resulting from the anisotropic case of the main fault (i.e., $\kappa_{MF_vertical}/\kappa_{MF_horizontal} = 10^{-13} \text{ m}^2/10^{-15} \text{ m}^2$), provide the most realistic explanation for the kilometer-scale elevated temperature of 270 ~ 300 °C in the Piesberg Quarry. Our study proves that fractured/faulted zones in tight sandstone reservoirs (a common petroleum reservoir play type) and associated thermal anomalies may be preferred geothermal reservoirs in sedimentary basins worldwide (e.g., LSB). Our 3D numerical model also provides predictive tools for the origin, location, scale, and magnitude of exploitable geothermal reservoirs. More processes (i.e., chemistry and (geo-)mechanics) should be investigated in the further step for the fully coupled transport mechanisms in faulted tight sandstones.

Code and data availability. The numerical codes and data are available upon request to the first author.

Author contributions. GY, BB, and RE investigated the project and designed the methodology. GY performed the simulations and validation and visualized the results. TK supervised the project. GY prepared the manuscript with contributions from all co-authors.

Conflicts of interest. The authors declare that they have no conflict of interest.

Acknowledgments. This study is part of the subtopic “Geoenergy” in the program “MTET - Materials and Technologies for the Energy Transition” of the Helmholtz Association. The support from the program is gratefully acknowledged. Guoqiang Yan is funded by the China Scholarship Council (Grant No. 201709370076). We thank Ali Dashti and Fabian Nitschke (Karlsruhe Institute of Technology) for their assistance in reviewing the manuscript as well as Maziar Gholami Korzani (Queensland University of Technology) for his contribution in the early stages of this study.

480 Reference

- © Microsoft: Piesberg, Osnabrück, Federal Republic of Germany, 2015.
- Achtziger-Zupančič, P., Loew, S., and Hiller, A.: Factors controlling the permeability distribution in fault vein zones surrounding granitic intrusions (Ore Mountains/Germany), *J. Geophys. Res. Solid Earth*, <https://doi.org/10.1002/2016JB013619>, 2017a.
- 485 Achtziger-Zupančič, P., Loew, S., and Mariéthoz, G.: A new global database to improve predictions of permeability distribution in crystalline rocks at site scale, *J. Geophys. Res. Solid Earth*, 122, 3513–3539, <https://doi.org/10.1002/2017JB014106>, 2017b.
- Andrews, Day, J., and Marshall, J. E.: A thermal anomaly associated with the Rusey Fault and its implications for fluid movements, *PROCEEDINGS-USSHER SOCIETY*, 9, 68–71, 1996.
- 490 Bächler, D., Kohl, T., and Rybach, L.: Impact of graben-parallel faults on hydrothermal convection—Rhine Graben case study, *Physics and Chemistry of the Earth, Parts A/B/C*, 28, 431–441, [https://doi.org/10.1016/S1474-7065\(03\)00063-9](https://doi.org/10.1016/S1474-7065(03)00063-9), 2003.



- Baillieux, P., Schill, E., Edel, J.-B., and Mauri, G.: Localization of temperature anomalies in the Upper Rhine Graben: insights from geophysics and neotectonic activity, *International Geology Review*, 55, 1744–1762, <https://doi.org/10.1080/00206814.2013.794914>, 2013.
- 495 Baldschuhn, R. and Kockel, F.: The Osning Lineament at the southern fringe of the Lower Saxony Basin, *zdgg_alt*, 150, 673–695, <https://doi.org/10.1127/zdgg/150/2000/673>, 2000.
- Baldschuhn, R., Binot, F., Fleig, S., and Kockel, F.: *Geotektonischer Atlas von Nordwest-Deutschland und dem deutschen Nordsee-Sektor*, 2001.
- 500 Beck, A. E., Garven, G., and Stegena, L. (Eds.): *Hydrogeological Regimes and Their Subsurface Thermal Effects*, Geophysical Monograph Series, American Geophysical Union, Washington, D. C., 1989.
- Becker, I., Busch, B., Koehrer, B., Adelman, D., and Hilgers, C.: Reservoir quality evolution of Upper Carboniferous (Westphalian) tight gas sandstones, Lower Saxony Basin, NW Germany, *Journal of Petroleum Geology*, 42, 371–392, <https://doi.org/10.1111/jpg.12742>, 2019.
- 505 Bruhn, R. L., Parry, W. T., Yonkee, W. A., and Thompson, T.: Fracturing and hydrothermal alteration in normal fault zones, *PAGEOPH*, 142, 609–644, <https://doi.org/10.1007/BF00876057>, 1994.
- Bruns, B., Di Primio, R., Berner, U., and Littke, R.: Petroleum system evolution in the inverted Lower Saxony Basin, northwest Germany: a 3D basin modeling study, *Geofluids*, 13, 246–271, <https://doi.org/10.1111/gfl.12016>, 2013.
- 510 *Geotektonischer Atlas von Nordwest-Deutschland und dem deutschen Nordsee-Sektor: Strukturen, Strukturentwicklung, Paläogeographie*, Geologisches Jahrbuch Reihe A, Allgemeine und regionale Geologie Bundesrepublik Deutschland und Nachbargebiete, Tektonik, Stratigraphie, Paläontologie, 153, Buch, Schweizerbart, Stuttgart, 88 pp., 2001.
- Busch, B., Becker, I., Koehrer, B., Adelman, D., and Hilgers, C.: Porosity evolution of two Upper Carboniferous tight-gas-fluvial sandstone reservoirs: Impact of fractures and total cement volumes on reservoir quality, *Marine and Petroleum Geology*, 100, 376–390, <https://doi.org/10.1016/j.marpetgeo.2018.10.051>, 2019.
- 515 Cherubini, Y., Cacace, M., Blöcher, G., and Scheck-Wenderoth, M.: Impact of single inclined faults on the fluid flow and heat transport: results from 3-D finite element simulations, *Environ Earth Sci*, 70, 3603–3618, <https://doi.org/10.1007/s12665-012-2212-z>, 2013.
- Clauser, C. and Villinger, H.: Analysis of conductive and convective heat transfer in a sedimentary basin, demonstrated for the Rheingraben, *Geophysical Journal International*, 100, 393–414, <https://doi.org/10.1111/j.1365-246X.1990.tb00693.x>, 1990.
- 520 David, F., Albertsen, M., and Blohm, M.: *Sedimentologie und Beckenanalyse im Westfal C und D des nordwestdeutschen Beckens*, DGMK, 1990.
- Egert, R., Nitschke, F., Gholami Korzani, M., and Kohl, T.: Stochastic 3D Navier - Stokes Flow in Self - Affine Fracture Geometries Controlled by Anisotropy and Channeling, *Geophys Res Lett*, 48, <https://doi.org/10.1029/2020GL092138>, 2021.
- 525 Egert, R., Korzani, M. G., Held, S., and Kohl, T.: Implications on large-scale flow of the fractured EGS reservoir Soultz inferred from hydraulic data and tracer experiments, *Geothermics*, 84, 101749, <https://doi.org/10.1016/j.geothermics.2019.101749>, 2020.
- Elderfield, H., Wheat, C. G., Mottl, M. J., Monnin, C., and Spiro, B.: Fluid and geochemical transport through oceanic crust: a transect across the eastern flank of the Juan de Fuca Ridge, *Earth and Planetary Science Letters*, 172, 151–165, [https://doi.org/10.1016/S0012-821X\(99\)00191-0](https://doi.org/10.1016/S0012-821X(99)00191-0), 1999.
- 530 Emry, E. L., Nyblade, A. A., Horton, A., Hansen, S. E., Julià, J., Aster, R. C., Huerta, A. D., Winberry, J. P., Wiens, D. A., and Wilson, T. J.: Prominent thermal anomalies in the mantle transition zone beneath the Transantarctic Mountains, *Geology*, 48, 748–752, <https://doi.org/10.1130/G47346.1>, 2020.
- Farrell, N., Healy, D., and Taylor, C. W.: Anisotropy of permeability in faulted porous sandstones, *Journal of Structural Geology*, 63, 50–67, <https://doi.org/10.1016/j.jsg.2014.02.008>, 2014.



- Gholami Korzani, M., Held, S., and Kohl, T.: Numerical based filtering concept for feasibility evaluation and reservoir performance enhancement of hydrothermal doublet systems, *Journal of Petroleum Science and Engineering*, 190, 106803, <https://doi.org/10.1016/j.petrol.2019.106803>, 2020.
- Gholami Korzani, M., Nitschke, F., Held, S., and Kohl, T.: The Development of a Fully Coupled Wellbore-Reservoir Simulator for Geothermal Application, *Transactions*, 43, 927–936, 2019.
- 540 Guillou-Frottier, L., Duwiquet, H., Launay, G., Taillefer, A., Roche, V., and Link, G.: On the morphology and amplitude of 2D and 3D thermal anomalies induced by buoyancy-driven flow within and around fault zones, *Solid Earth*, 11, 1571–1595, <https://doi.org/10.5194/se-11-1571-2020>, 2020.
- Guillou-Frottier, L., Carré, C., Bourguin, B., Bouchot, V., and Genter, A.: Structure of hydrothermal convection in the Upper Rhine Graben as inferred from corrected temperature data and basin-scale numerical models, *Journal of Volcanology and Geothermal Research*, 256, 29–49, <https://doi.org/10.1016/j.jvolgeores.2013.02.008>, 2013.
- 545 Haarmann, E.: Die geologischen Verhältnisse des Piesbergs-Sattels bei Osnabrück, Königl. Geologische Landesanstalt, 1909.
- Harcouët-Menou et al.: Hydrothermal convection in and around mineralized fault zones: insights from two- and three-dimensional numerical modeling applied to the Ashanti belt, Ghana, *Geofluids*, 9, 116–137, <https://doi.org/10.1111/j.1468-8123.2009.00247.x>, 2009.
- 550 Hinze, C.: Erläuterungen zu Blatt Nr. 3614 Wallenhorst, Geologische Karte von Niedersachsen, 1, 154, 1979.
- Huenges and Ledru (Ed.): Geothermal energy systems: Exploration, development and utilization, Online-Ausg, Wiley-VCH, Weinheim, 463 pp., 2010.
- 555 Ingebritsen, S. E. and Manning, C. E.: Geological implications of a permeability-depth curve for the continental crust, *Geol*, 27, 1107, [https://doi.org/10.1130/0091-7613\(1999\)027<1107:GIOAPD>2.3.CO;2](https://doi.org/10.1130/0091-7613(1999)027<1107:GIOAPD>2.3.CO;2), 1999.
- Jobmann, M. and Clauser, C.: Heat advection versus conduction at the KTB: possible reasons for vertical variations in heat-flow density, *Geophysical Journal International*, 119, 44–68, <https://doi.org/10.1111/j.1365-246X.1994.tb00912.x>, 1994.
- 560 Kämmlin, M., Dietl, C., and Stollhofen, H.: The Franconian Basin thermal anomaly: testing its origin by conceptual 2-D models of deep-seated heat sources covered by low thermal conductivity sediments, *Int J Energy Environ Eng*, 10, 389–412, <https://doi.org/10.1007/s40095-019-00315-2>, 2019.
- Kohl, T., Bächler, D., and Rybach, L.: Steps towards a comprehensive thermo-hydraulic analysis of the HDR test site Soultz-sous-Forêts, in: *Proceedings World Geothermal Congress*, 2671–2676, 2000.
- Kombrink, H., Besly, B., Collinson, J., Jäger, H., Drozdowski, G., Dusat, M., Hoth, P., Pagnier, H., Stemmerik, L., Waksmondzka, M., and Wrede, V.: Carboniferous, *Petroleum Geological Atlas of the Southern Permian Basin Area*, 81–99, 2010.
- 565 Kuang, X. and Jiao, J. J.: An integrated permeability-depth model for Earth's crust, *Geophys Res Lett*, 41, 7539–7545, <https://doi.org/10.1002/2014GL061999>, 2014.
- Kühn, M. and Gessner, K.: Testing Hypotheses for the Mount Isa Copper Mineralisation with Numerical Simulations, *Surv Geophys*, 30, 253–268, <https://doi.org/10.1007/s10712-009-9064-4>, 2009.
- 570 Lampe, C. and Person, M.: Episodic hydrothermal fluid flow in the Upper Rhinegraben (Germany), *Journal of Geochemical Exploration*, 69–70, 37–40, [https://doi.org/10.1016/S0375-6742\(00\)00049-2](https://doi.org/10.1016/S0375-6742(00)00049-2), 2000.
- Liewig, N. and Clauer, N.: K-Ar dating of varied microtextural illite in Permian gas reservoirs, northern Germany, *Clay miner.*, 35, 271–281, <https://doi.org/10.1180/000985500546648>, 2000.
- 575 Linstrom, P. J. and Mallard, W. G.: The NIST Chemistry WebBook: A Chemical Data Resource on the Internet, *J. Chem. Eng. Data*, 46, 1059–1063, <https://doi.org/10.1021/je000236i>, 2001.
- López, D. L. and Smith, L.: Fluid flow in fault zones: Influence of hydraulic anisotropy and heterogeneity on the fluid flow and heat transfer regime, *Water Resour. Res.*, 32, 3227–3235, <https://doi.org/10.1029/96WR02101>, 1996.



- López, D. L. and Smith, L.: Fluid flow in fault zones: analysis of the interplay of convective circulation and topographically driven Groundwater Flow, *Water Resour. Res.*, 31, 1489–1503, <https://doi.org/10.1029/95WR00422>, 1995.
- Magri, F., Möller, S., Inbar, N., Möller, P., Raggad, M., Rödigier, T., Rosenthal, E., and Siebert, C.: 2D and 3D coexisting modes of thermal convection in fractured hydrothermal systems - Implications for transboundary flow in the Lower Yarmouk Gorge, *Marine and Petroleum Geology*, 78, 750–758, <https://doi.org/10.1016/j.marpetgeo.2016.10.002>, 2016.
- Magri, F., Littke, R., Rodon, S., Bayer, U., and Urai, J. L.: Temperature fields, petroleum maturation and fluid flow in the vicinity of salt domes, *Dynamics of Complex Intracontinental Basins: The Central European Basin System*, 323–344, 2008.
- Malkovsky, V. I. and Magri, F.: Thermal convection of temperature-dependent viscous fluids within three-dimensional faulted geothermal systems: Estimation from linear and numerical analyses, *Water Resour. Res.*, 52, 2855–2867, <https://doi.org/10.1002/2015WR018001>, 2016.
- Manning, C. E. and Ingebritsen, S. E.: Permeability of the continental crust: Implications of geothermal data and metamorphic systems, *Rev. Geophys.*, 37, 127–150, <https://doi.org/10.1029/1998RG900002>, 1999.
- McKenna, J. R. and Blackwell, D. D.: Numerical modeling of transient Basin and Range extensional geothermal systems, *Geothermics*, 33, 457–476, <https://doi.org/10.1016/j.geothermics.2003.10.001>, 2004a.
- McKenna, J. R. and Blackwell, D. D.: Numerical modeling of transient Basin and Range extensional geothermal systems, *Geothermics*, 33, 457–476, <https://doi.org/10.1016/j.geothermics.2003.10.001>, 2004b.
- Moeck, I. S.: Catalog of geothermal play types based on geologic controls, *Renewable and Sustainable Energy Reviews*, 37, 867–882, <https://doi.org/10.1016/j.rser.2014.05.032>, 2014.
- Nield, D. A. and Bejan, A.: *Convection in porous media*, Springer, 2017.
- O’Brien, J. J. and Lerche, I.: Impact of heat flux anomalies around salt diapirs and salt sheets in the Gulf Coast on hydrocarbon maturity, *Gulf Coast Association of Geological Societies Transactions*, 38, 231–243, 1988.
- Panja, P., McLennan, J., and Green, S.: Influence of permeability anisotropy and layering on geothermal battery energy storage, *Geothermics*, 90, 101998, <https://doi.org/10.1016/j.geothermics.2020.101998>, 2021.
- Parry, W.: Fault-fluid compositions from fluid-inclusion observations and solubilities of fracture-sealing minerals, *Tectonophysics*, 290, 1–26, [https://doi.org/10.1016/S0040-1951\(98\)00013-4](https://doi.org/10.1016/S0040-1951(98)00013-4), 1998.
- Permann, C. J., Gaston, D. R., Andrš, D., Carlsen, R. W., Kong, F., Lindsay, A. D., Miller, J. M., Peterson, J. W., Slaughter, A. E., Stogner, R. H., and Martineau, R. C.: MOOSE: Enabling massively parallel multiphysics simulation, *SoftwareX*, 11, 100430, <https://doi.org/10.1016/j.softx.2020.100430>, 2020.
- Przybycin, A. M., Scheck-Wenderoth, M., and Schneider, M.: The origin of deep geothermal anomalies in the German Molasse Basin: results from 3D numerical models of coupled fluid flow and heat transport, *Geotherm Energy*, 5, <https://doi.org/10.1186/s40517-016-0059-3>, 2017.
- Saar, M. O. and Manga, M.: Depth dependence of permeability in the Oregon Cascades inferred from hydrogeologic, thermal, seismic, and magmatic modeling constraints, *J. Geophys. Res.*, 109, <https://doi.org/10.1029/2003JB002855>, 2004.
- Schilling, O., Sheldon, H. A., Reid, L. B., and Corbel, S.: Hydrothermal models of the Perth metropolitan area, Western Australia: implications for geothermal energy, *Hydrogeol J*, 21, 605–621, <https://doi.org/10.1007/s10040-012-0945-0>, 2013.
- Senglaub, Y., Littke, R., and Brix, M. R.: Numerical modelling of burial and temperature history as an approach for an alternative interpretation of the Bramsche anomaly, *Lower Saxony Basin, Int J Earth Sci (Geol Rundsch)*, 95, 204–224, <https://doi.org/10.1007/s00531-005-0033-y>, 2006.
- Sheldon, H. A., Florio, B., Trefry, M. G., Reid, L. B., Ricard, L. P., and Ghori, K. A. R.: The potential for convection and implications for geothermal energy in the Perth Basin, Western Australia, *Hydrogeol J*, 20, 1251–1268, <https://doi.org/10.1007/s10040-012-0886-7>, 2012.
- Smith, L. and Chapman, D. S.: On the thermal effects of groundwater flow: 1. Regional scale systems, *J. Geophys. Res.*, 88, 593, <https://doi.org/10.1029/JB088iB01p00593>, 1983.



- Tzoufka, K., Magri, F., Rödiger, T., Inbar, N., Shalev, E., Möller, P., Raggad, M., Rosenthal, E., and Siebert, C.: The effect of hydraulic anisotropies on intensely exploited groundwater resources: the numerical evaluation of a hydrothermal transboundary aquifer system in the Middle East, *Hydrogeol J*, 26, 2875–2890, <https://doi.org/10.1007/s10040-018-1827-x>, 2018.
- 625 Will, P., Lüders, V., Wemmer, K., and Gilg, H. A.: Pyrophyllite formation in the thermal aureole of a hydrothermal system in the Lower Saxony Basin, Germany, *Geofluids*, 16, 349–363, <https://doi.org/10.1111/gfl.12154>, 2016.
- Wisian, K. W. and Blackwell, D. D.: Numerical modeling of Basin and Range geothermal systems, *Geothermics*, 33, 713–741, <https://doi.org/10.1016/j.geothermics.2004.01.002>, 2004a.
- 630 Wisian, K. W. and Blackwell, D. D.: Numerical modeling of Basin and Range geothermal systems, *Geothermics*, 33, 713–741, <https://doi.org/10.1016/j.geothermics.2004.01.002>, 2004b.
- Wuestefeld, P., Hilgers, C., Koehrer, B., Hoehne, M., Steindorf, P., Schurk, K., Becker, S., and Bertier, P.: Reservoir heterogeneity in Upper Carboniferous tight gas sandstones: Lessons learned from an analog study, in: *SPE/EAGE European Unconventional Resources Conference and Exhibition*, 1–10, 2014.
- 635 Wüstefeld, P., Hilse, U., Koehrer, B., Adelmann, D., and Hilgers, C.: Critical evaluation of an Upper Carboniferous tight gas sandstone reservoir analog: Diagenesis and petrophysical aspects, *Marine and Petroleum Geology*, 86, 689–710, <https://doi.org/10.1016/j.marpetgeo.2017.05.034>, 2017a.
- Wüstefeld, P., Hilse, U., Lüders, V., Wemmer, K., Koehrer, B., and Hilgers, C.: Kilometer-scale fault-related thermal anomalies in tight gas sandstones, *Marine and Petroleum Geology*, 86, 288–303, <https://doi.org/10.1016/j.marpetgeo.2017.05.015>, 2017b.
- 640 Zwingmann, H., Clauer, N., and Gaupp, R.: Structure-related geochemical (REE) and isotopic (K-Ar, Rb-Sr, $\delta^{18}\text{O}$) characteristics of clay minerals from Rotliegend sandstone reservoirs (Permian, northern Germany), *Geochimica et Cosmochimica Acta*, 63, 2805–2823, [https://doi.org/10.1016/S0016-7037\(99\)00198-2](https://doi.org/10.1016/S0016-7037(99)00198-2), 1999.
- Zwingmann, H., Clauer, N., and Gaupp, R.: Timing of fluid flow in a sandstone reservoir of the north German Rotliegend (Permian) by K-Ar dating of related hydrothermal illite, *Geological Society, London, Special Publications*, 144, 91–106, <https://doi.org/10.1144/GSL.SP.1998.144.01.07>, 1998.
- 645